INORGANIC CHEMISTRY FRONTIERS

RESEARCH ARTICLE

View Article Online
View Journal | View Issue

Cite this: *Inorg. Chem. Front.*, 2026, **13**, 4638

Spin-crossover tuning in synergistic luminescent Fe(II) coordination compounds *via* topochemical [4 + 4] photocycloaddition of an anthracene-based ligand

Matthias Schöbinger, *†[a] Martin Huber, †[a] Sophia Mundigler, †[a] Berthold Stöger, [b] Michael Reissner[c] and Peter Weinberger [a]

Coordination polymers (CPs) designed to couple spin crossover (SCO) and photoluminescence (PL) properties hold significant potential for sensor applications, enabling optical readout of spin states. We report the synthesis of the novel ligand **L1** (1-(anthracen-9-ylmethyl)-1*H*-tetrazole), which undergoes a reversible [4 + 4] photocycloaddition to form the head-to-tail dimer **L2** – a ditopic tetrazole ligand, key to the design of CPs. Utilizing these ligands, we synthesized a family of Fe(II) anthracene based SCO-PL coordination compounds with varying dimensionalities: 0D ([Fe**L1**$_4$(CH_3CN)$_2$](ClO_4)$_2$·2CH_3CN, **1**), 1D ([Fe**L1**$_2$**L2**(CH_3CN)$_2$](ClO_4)$_2$·2CH_3CN, **2**) and 2D ([Fe**L2**$_2$(CH_3CN)$_2$](ClO_4)$_2$·2CH_3CN, **3**). Notably, **L1** retains its photoreactivity after coordination in **1**, and the subsequent polymerization of **1** to **2** represents a rare example of a topochemical reaction. Magnetic studies confirmed thermally induced SCO behavior in all three coordination compounds (**1–3**), with increasing cooperativity correlating with greater structural rigidity. Variable-temperature PL spectra revealed an interplay between the spin transition and PL in **2** and **3**, showing PL quenching in the low-spin state, which diminishes as the high-spin state population increases. Our findings provide a platform to further develop synergistic SCO-PL CPs with tunable magneto-optical properties, paving the way for future applications.

Received 9th June 2025,
Accepted 2nd April 2026

DOI: 10.1039/d5qi01281c

rsc.li/frontiers-inorganic

Introduction

The spin crossover (SCO) phenomenon was first discovered by Cambi *et al.* (1931)[1] and describes the switch from a high-spin (HS) state to a low-spin (LS) state and *vice versa* of $3d^4$–$3d^7$ coordination compounds by external stimuli such as irradiation, temperature, or pressure, among others.[2–4] The spin transition is inherently accompanied by significant changes in the structural, optical, and magnetic properties of the coordination compound.[5–7]

Modern materials chemistry is focused on the combination of the SCO phenomenon with an additional property such as non-linear optics,[8] electrical conductivity,[9] chirality,[10] luminescence,[11–13] host–guest interactions,[14] *etc.*, which exhibit synergistic effects with the spin state of the compound. Multifunctional SCO systems hold great promise for molecular devices, including sensors, photonic instruments, actuators, and memory units.[15,16] In particular, coupling SCO materials with photoluminescence (PL) properties is a powerful strategy for applications in photonic switches,[17] thermometers,[18,19] and sensor devices,[20] as the intrinsic fluorescence signal provides superior contrast and sensitivity, enabling reliable remote readout of the spin state with high spatial and temporal resolution.[11,15,21]

Although a considerable amount of successful synergistic SCO-PL systems already exists in literature, the development of new SCO-PL systems remains a major challenge and often results in unpredictable changes or even loss of SCO and/or PL properties.[12,13]

One established approach is the design of molecular SCO-PL systems where the luminescent unit is part of the coordinating ligands, enabling unambiguous structure–property conclusions. Recent literature on molecular SCO-PL systems particularly often proposed mechanistic coupling to the Förster resonance energy transfer (FRET) mechanism – a non-radiative process that relies on spectral overlap between the absorption band of the SCO complex and the emission band of the luminophore. In contrast, radiative energy transfer

[a]*Institute of Applied Synthetic Chemistry, TU Wien, Getreidemarkt 9, 1060 Vienna, Austria. E-mail: matthias.schoebinger@tuwien.ac.at, peter.e163.weinberger@tuwien.ac.at*
[b]*X-Ray Center, TU Wien, Getreidemarkt 9/164, 1060 Vienna, Austria*
[c]*Institute of Solid State Physics, TU Wien, Wiedner Hauptstraße 8, 1040 Vienna, Austria*
†These authors contributed equally.

(emission-reabsorption) becomes more significant at longer distances between the SCO and PL units.[11] Moreover, although assessing the extent to which structural changes associated with the SCO process modulate emission beyond electronic coupling is challenging, their impact should not be underestimated.[22,23]

Anthracene, which is known for its high thermal stability, strong luminescence and charge transfer properties,[24–26] has already been successfully incorporated into SCO-PL systems.[27–31] In addition to these favorable characteristics, anthracene can undergo a reversible [4 + 4] photocycloaddition upon UV irradiation to form dianthracene. This transformation adheres to Schmidt's topochemical criteria, which require a precise molecular arrangement to facilitate dimerization.[32,33] However, in contrast to general topochemical polymerizations, which are increasingly being reported on,[34,35] only a few examples of coordination compounds featuring anthracene ligands have been reported to follow this reaction path.[36–40]

Photodimerization is particularly attractive in the design of novel coordination polymers (CPs), as it increases the number of network nodes and the system's dimensionality by linking molecules from adjacent complexes.[41,42] In the field of SCO, CPs are of special interest due to their inherent porosity, tunable functionalities, versatile design and pronounced cooperativity effects that influence their magnetic behavior.[43–45] While 1D SCO-PL CPs – predominantly based on triazole-derivatives as bridging ligands[19,23,30,46–51] – are well studied, the synthesis of 2D and 3D architectures remains challenging and relatively rare.

To the best of our knowledge, the photodimerization of anthracene has not yet been incorporated into SCO systems – an approach that could offer valuable insights into SCO modulation by increasing the dimensionality of the system and advancing the understanding of structure–property relationships.

In this work, we design and employ a ligand consisting of 1*H*-tetrazole (tz) as the coordinating unit and an anthracene moiety, linked *via* a CH_2 bridge to the N1 position of the tz, which can undergo photodimerization (Scheme 1). The advantages of N1-substituted tz for Fe(II) SCO complexes have been extensively demonstrated in our previous studies.[52–55] We combine the two remarkable properties of anthracene – luminescence and photodimerization – in a novel Fe(II) SCO-PL system. In this context, we aim to achieve a synergistic response, where the luminescence signal of anthracene is modulated by the spin state of Fe(II). Additionally, we seek to develop new topological variants of our targeted anthracene Fe(II) coordination compound through photodimerization of coordinated anthracene units.

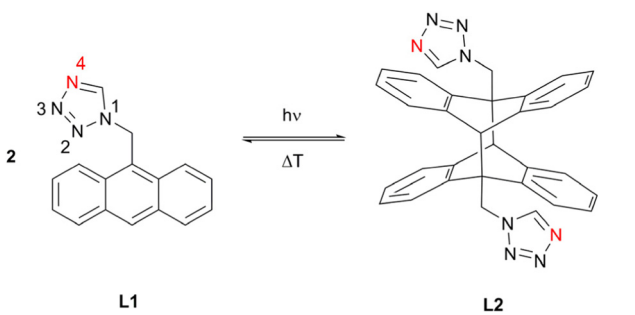

Scheme 1 Photoluminescence active ligands **L1** and **L2**, observed coordination site in red (*N*4-atom).

Results and discussion

Synthesis

The precursor of **L1**, anthracen-9-ylmethanamine, was synthesized following a previously reported protocol.[56] Subsequently, the amine group was converted to a tz moiety using a well-established tz synthesis method described in literature (Scheme S1).[57] The reactions outlined below are depicted in Scheme 2. **L1** is highly photoreactive and partially undergoes a [4 + 4] photocycloaddition shortly after synthesis, even in solid state and under ambient light, forming **L2**, which is the *trans*-dimer[58]/head-to-tail dimer[59] of **L1**. To prevent the formation of **L2** and the reaction of **L1** with oxygen, leading to *e.g.*, peroxides,[59] **L1** has to be stored strictly under an atmosphere of argon and protected from light. A controlled synthesis of **L2** in solution is achieved quantitatively by irradiation with a 365 nm LED at room temperature (rt). However, in the solid state the conversion stops reproducibly at 50%, after irradiation with the same wavelength. We believe that this is due to the fact that the powder of **L1** consists of different polymorphs (*vide infra*),[60] which do not all possess the correct spatial arrangement[61] of the anthracene moieties to perform this dimerization reaction. The [4 + 4] photocycloaddition of **L1** is quantitatively reversible by heating **L2** in solution to 150 °C for 10 min. The powder of **L2** shows thermal stability until heating to 175 °C (Fig. S52–56). As expected, **L1** and **L2** have entirely different solubility properties.[59,61] **L1** shows good solubility *e.g.*, in CH_2Cl_2 or CH_3CN, in contrast to **L2** which is hardly soluble in any common solvents except dimethyl sulfoxide (DMSO).

The heteroleptic coordination compound **1** with acetonitrile (CH_3CN) as co-ligand in the apical positions is easily obtained by mixing **L1** with $Fe(ClO_4)_2{\cdot}6H_2O$ in CH_3CN and stirring at elevated temperature (40 °C) over night. **1** was precipitated and washed with diethyl ether (Et_2O). Interestingly, the photoreactivity of **L1** is retained after complexation, as **1** undergoes conversion to **2**, a 1D CP, under ambient light irradiation. This retained photoreactivity in coordination compounds is rarely shown in literature.[37] Controlled irradiation of **1** in the solid state with a 365 nm LED at rt results in the complete conversion of **1** and the exclusive formation of **2**. This [4 + 4] photocycloaddition of the coordinated ligand **L1** proceeds only in one direction of the equatorial plane and can be explained by the spatial arrangement of the anthracene moieties in the crystal packing of **1** (*vide infra*). Besides this solid-state reaction, **2** can

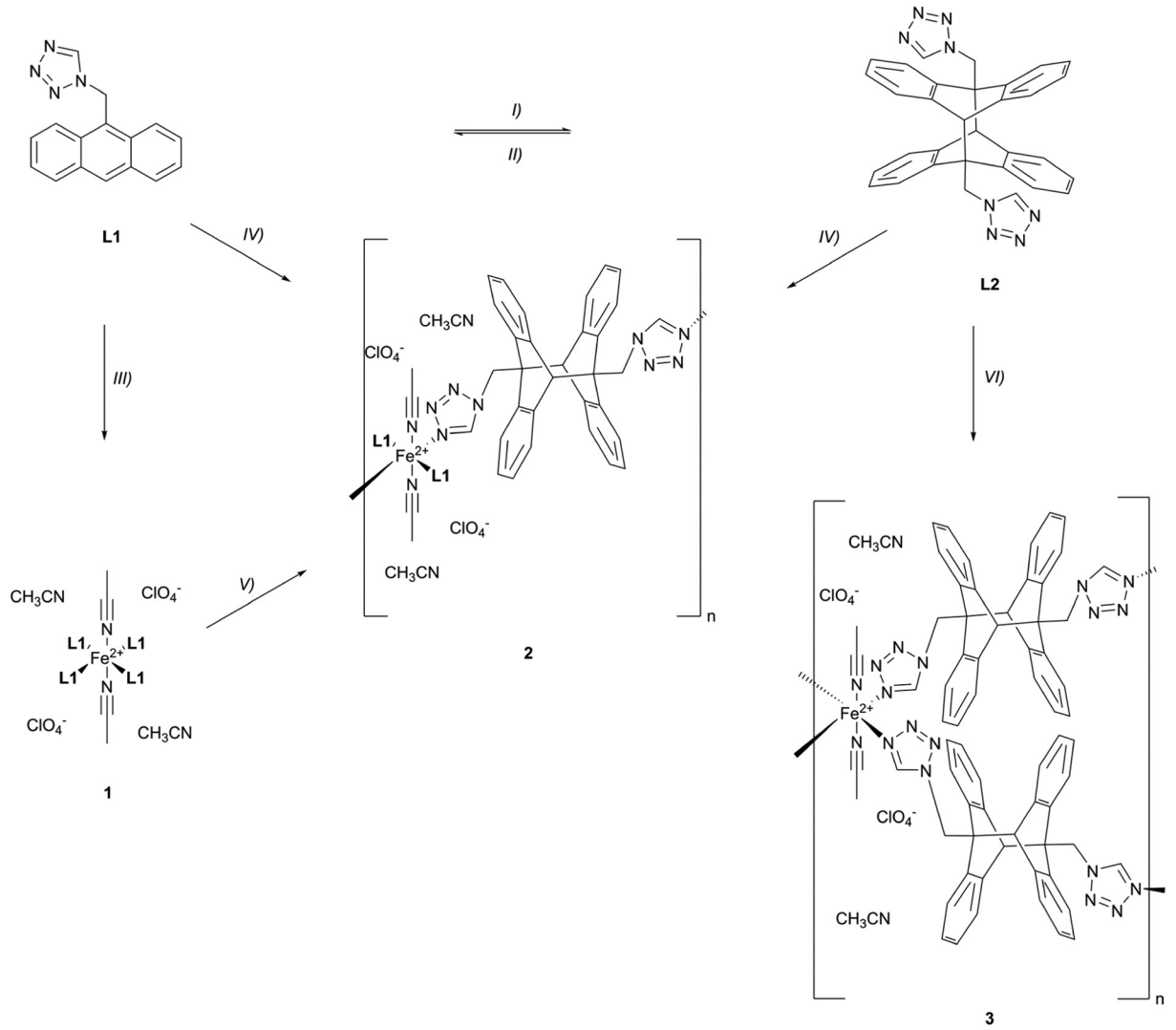

Scheme 2 Synthesis of ligand **L2** and coordination compounds **1–3**, reagents and conditions: (I) 365 nm, CH_2Cl_2, rt, 6 h, quant.; (II) DMSO, 150 °C, 3 h, quant.; (III) $Fe(ClO_4)_2{\cdot}6H_2O$, CH_3CN, 40 °C, o.n., 59.3%; (IV) **L1** : **L2** = 2 : 1, $Fe(ClO_4)_2{\cdot}6H_2O$, CH_3CN, 40 °C, o.n., 60.9%; (V) **1** in solid state, 365 nm, rt, 3 h, quant.; (VI) $Fe(ClO_4)_2{\cdot}6H_2O$, CH_3CN, 40 °C, o.n., 70.0%.

also be synthesized *via* a classical coordination reaction using two equivalents of **L1** and one equivalent of **L2**, with the same conditions applied as those used for the synthesis of **1**. It has to be mentioned that **L2** shows no thermal reversion of the [4 + 4] photocycloaddition under these complexation conditions (40 °C).

In a similar manner, coordination compound **3**, a 2D CP, is obtained when only two equivalents of **L2** are used.

Crystal structures

The single crystals (SCs) of all coordination compounds (**1–3**) and the non-solvate of **L2** (**L2-ns**) as well as the CH_3CN solvate of **L2** (**L2**·2CH_3CN, **L2-s1**) were obtained by slow evaporation at rt under an atmosphere of argon, using CH_3CN (CH_3CN : acetone = 1 : 1 for **3**) as the solvent. The SCs of the two polymorphs of **L1** (**L1-p1** and **L1-p2**) and a second solvate of **L2** (**L2**·2CH_3OH, **L2-s2**) were grown by vapor diffusion of an antisolvent (Et_2O) into saturated solutions of the ligands in CH_3OH (**L1-p1** and **L2-s2**) or CH_3CN (**L1-p2**) at rt.

The two polymorphs of **L1** found during this study crystallize in the triclinic $P\bar{1}$ space group (**L1-p1**, Fig. S26–29) and in the trigonal $P3_1/P3_2$ space group (**L1-p2**, Fig. S30 and 31). The asymmetric unit of **L1-p1** consists of two conformers of **L1**, which mainly differ in the orientation of the tz moiety towards the anthracene plane. This variation in the orientation of the tz group, which is connected *via* a methylene (CH_2) bridge to a larger rigid planar moiety, has been reported previously.[62] In both conformers, the tetrazolic C-atom is oriented away from the anthracene plane; however, the torsion angle between the tz and the anthracene is different (60.3(7)° *vs.* 70.0(7)°, Fig. 1).

L1-p2 features only one conformer of **L1** with a very similar inclination of the tz moiety (torsion angle: 61.0(7)°). In **L1-p1** and **L1-p2** the molecules stack in a head-to-head coplanar fashion along the crystallographic *a*- and *c*-axis, whereby adja-

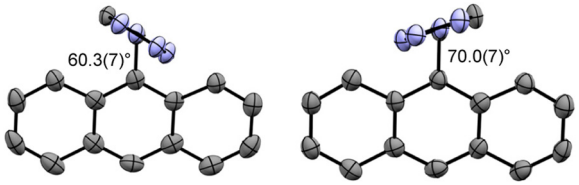

Fig. 1 Top view of the molecular structure of the two different conformers in **L1-p1**, showing the orientation of the tz moiety (ellipsoids: 50% probability level; atom color code: grey···C, blue···N; H-atoms are omitted for clarity).

cent molecules are related by lattice translation. The distance between the perfectly coplanar L.S. planes of the anthracene moieties are 3.427(7) Å and 3.467(7) Å (**L1-p1**), respectively 3.481(6) Å (**L1-p2**).

Both polymorphs of **L1** (**L1-p1** and **L1-p2**) feature a C–H···N hydrogen bond network[63] forming infinite chains along the [100] direction and about the $3_1/3_2$ axis, respectively.

XRPD measurements reveal that the powder obtained after the synthesis of **L1** contains not only these two polymorphs (SI XRPD Measurements). This is in good agreement with the results found during the solid-state [4 + 4] photocycloaddition of this powder, which is only partially possible (*vide supra*). Of the four prerequisites for dimerization – co-planar arrangement, short intermolecular distances (<4.2 Å), sufficient overlap and head-to-tail arrangement between adjacent anthracene moieties[32,37,61,64] – only the first two are fulfilled for **L1-p1** and **L1-p2**. Moreover, a SC of **L1-p2** mounted on the diffractometer was directly irradiated overnight with the aforementioned 365 nm LED. Although the lattice parameters were determined at regular intervals, no photodimerization was observed. This suggests the existence of other, as-yet-undiscovered polymorphs, comprising at least 50% of the powder sample.

Besides the non-solvate of **L2** (**L2-ns**, Fig. 2), an acetonitrile solvate (**L2-s1**, Fig. S33) and a methanol solvate (**L2-s2**, Fig. S34) were found, which all crystallize in the triclinic $P\bar{1}$ space group. In contrast to **L1** in all three cases the tetrazolic C-atom is oriented towards the anthracene dimer. However, the torsion angle between the tz and the anthracene dimer in **L2-s1**, **L2-s2** and one of the two crystallographically independent molecules of **L2-ns** is very similar, measuring 15.40(18)°, 16.7(5)° and 16.0(7)°, respectively. The other **L2** molecule of **L2-ns** shows a torsion angle of 5.7(6)°. The loss of aromaticity in **L2** is clearly indicated by the large angle between the mean planes of the outer C_6 rings of the dimer, which depends on the conformer and ranges between approx. 39° and 52°. According to XRPD, the thoroughly dried bulk powder of **L2** is single-phase and corresponds to **L2-ns**.

For comparison reasons, all Fe(II)–SCO coordination compounds (**1–3**) were measured at the lowest possible measuring temperature (100 K) of the used SC-XRD setup (SI). At this temperature **1–3** are nearly completely in the HS state.

Coordination compound **1** crystallizes in the triclinic $P\bar{1}$ space group and for each mononuclear Fe(II) complex two non-

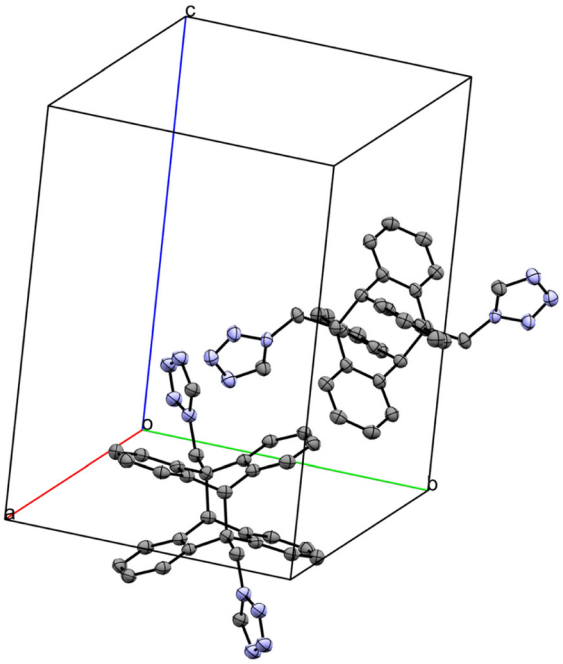

Fig. 2 Crystal packing of **L2-ns**, showing the two different conformers of **L2** (ellipsoids: 50% probability level; atom color code: grey···C, blue···N; H-atoms are omitted for clarity).

coordinating anions (ClO_4^-) and two molecules of CH_3CN are embedded in the crystal lattice (Fig. S36 and S38). The mononuclear complex of **1** has an octahedral geometry and is heteroleptic, due to the high steric demand[65] of **L1**, with two CH_3CN molecules acting as co-ligands in the apical positions (Fig. 3).

This was also demonstrated in earlier investigations with tz ligands of comparable size.[66] The distance between the coordi-

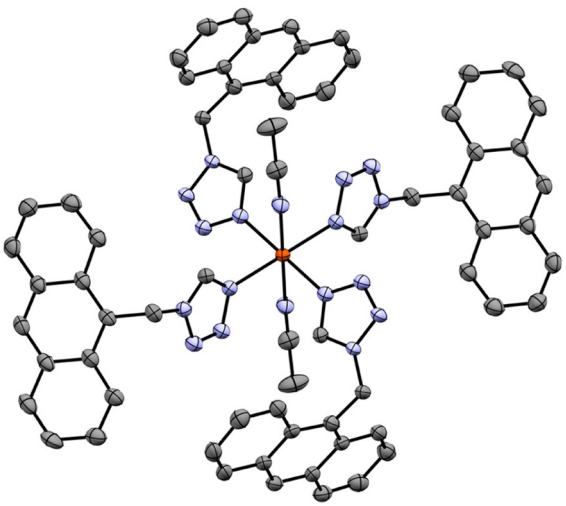

Fig. 3 Molecular structure of the mononuclear complex of coordination compound **1** (ellipsoids: 50% probability level; atom color code: grey···C, blue···N, orange···Fe; H-atoms, solvate molecules and anion molecules are omitted for clarity).

nating N9-atom of the co-ligand and the central atom (Fe1) is 2.141(3) Å. The CH_3CN molecules are not arranged along the ideal apical axis, but show a deviation (Fe1–N9–C33 157.2(3)°), which is also described in literature for comparable compounds.[67] In the equatorial plane four molecules of **L1** (two different conformers in *cis* arrangement) coordinate *via* their tetrazolic *N*4-atom (the italicized numbered N-atoms correspond to the tetrazole numbering system in Scheme 1) to the central atom with a distance of 2.195(3) Å (N4–Fe1) and 2.162 (3) Å (N8–Fe1), which is well within the range of literature known tz–Fe(II)–SCO systems in the HS state.[52,68] These distances are significantly longer than that between the coordinating N-atom of the co-ligand and the Fe-atom, resulting in a distorted octahedral geometry, as also reported in the literature.[67,69] The two conformers of **L1** differ in the orientation of the tz moiety relative to the anthracene plane, with torsion angles of 7.8(5)° (tetrazolic C32-atom directed towards the anthracene plane) and 74.7(4)° (tetrazolic C16-atom oriented away from the anthracene plane), respectively. In the crystal packing of **1**, neighboring mononuclear complexes are ordered in such a way that adjacent **L1** molecules are arranged in a coplanar, head-to-tail fashion. The centroid-to-centroid distance between the anthracene moieties of the two different conformers of **L1** differs, measuring 3.768 Å and 4.359 Å (Fig. 4). Moreover, in the latter case, the anthracene planes exhibit a significantly greater displacement relative to one other.

Coordination compound **2**, a 1D CP, crystallizes in the triclinic $P\bar{1}$ space group and extends along the [1$\bar{1}$0] direction. The building block of the infinite chain consists of an Fe(II)-atom, which is coordinated by three different ligands in an octahedral geometry. In the apical positions, two molecules of the co-ligand (CH_3CN) coordinate to the Fe center, with an N9–Fe1 bond length of 2.1288(19) Å. Like in **1**, there is a deviation from the ideal apical axis (Fe1–N9–C33 165.95(18)°). The equatorial plane is formed by two molecules of **L1** and two molecules of **L2**, arranged in *trans* configuration, each coordinating through the tetrazolic N4-atom. The N8-atom of **L1** in **2** shows a nearly identical distance to the Fe1-atom as in **1** (2.1653(18) Å). However, the same distance for **L2** is with 2.1313 (18) Å (N4–Fe1) a little bit shorter. The connection between these building blocks is established through the second tz moiety of **L2**, which also coordinates *via* the *N*4-atom and functions as bridging ligand (Fig. 5 and Fig. S40–S43).

The solid-state reaction of **1** to **2** occurs not only in powder form (*vide supra*) but also as a SC-to-SC transformation at 250 K. The reaction was carried out by irradiating a SC of **1** with a 365 nm LED while mounted on the SC diffractometer. Data was collected before, during and after the polymerization process. Images documenting this procedure are provided in the SI; however, the image taken after irradiation shows fragmentation of the SC, which is expected due to the metric distortion of the unit cell (Fig. S49–S51). This solid-state polymerization can be classified as topochemical reaction, a subgroup of topotactic reactions. This is based on the fact that the orientation of **2** is not only determined by the orientation of **1**, but in particular the symmetry of the educt is retained.[70]

The transformation initiates a contraction in the polymerization direction from an Fe-to-Fe distance of 15.4568 Å in **1** to 14.8155(5) Å in **2**. Comparison of the crystal structures of **1** and **2** reveals that only one of the two conformers of **L1** in **1** undergoes the [4 + 4] photocycloaddition. This conformer features an approximately 14% shorter centroid-to-centroid distance (3.768 Å) and a more extensive overlap with its neighboring **L1** molecule. Additionally, we propose that this conformer has a more favorable spatial arrangement of the tz relative to the anthracene moiety (torsion angle: 7.8(5)°, with the tetrazolic C-atom oriented toward the anthracene plane), which facili-

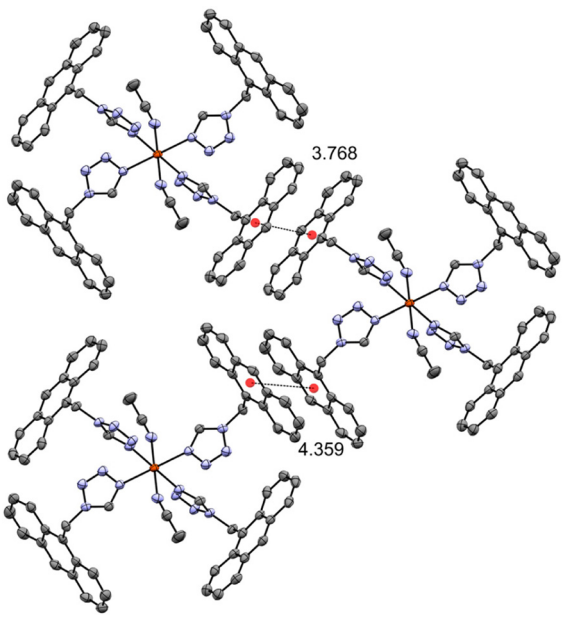

Fig. 4 Crystal packing of **1** with co-planar arrangement of anthracene moieties of the ligand **L1** of adjacent mononuclear complexes (ellipsoids: 50% probability level; atom color code: grey···C, blue···N, orange···Fe; H-atoms, solvate molecules and anion molecules are omitted for clarity; centroid-to-centroid distance shown as dotted line and given in Å).

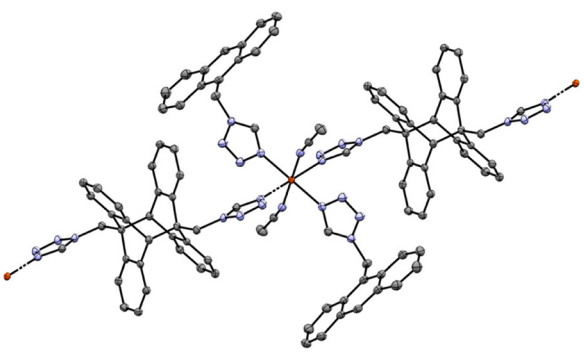

Fig. 5 Molecular structure of the 1D coordination polymer chain of coordination compound **2**, showing the bridging coordination mode of **L2** (ellipsoids: 50% probability level; atom color code: grey···C, blue···N, orange···Fe; H-atoms, solvate molecules and anion molecules are omitted for clarity).

tates the photodimerization to **L2** (Fig. 2). This assumption is based on the observation that all **L2** molecules found in the various solvatomorphs (**L2-ns**, **L2-s1** and **L2-s2**) and in the coordination compounds **2** and **3** exhibit small torsion angles (<40°), with the tetrazolic C-atom oriented towards the anthracene plane. We also assume that this is the reason why a further reaction to a 2D polymer is not possible. Moreover, the photopolymerization from **1** to **2** increases the centroid-to-centroid distance between the unreacted **L1** molecule from 4.359 Å to 5.372 Å and the previously coplanar arrangement of the anthracene moiety becomes distorted (Fig. S44).

Crystallization of coordination compound **3** proved challenging due to its low solubility, which was expected based on its polymeric structure. Nevertheless, by employing a mixture of acetone and CH_3CN and through extensive trial and error, a SC suitable for structural analysis was obtained. Although the crystal quality is limited, it allows for structural elucidation and is provided in the SI.

3 (Fig. S45–S48), a 2D CP, crystallizes in the triclinic $P\bar{1}$ space group and extends parallel to the $(1\bar{1}0)$ plane. The Fe(II)-atom is coordinated by four molecules of **L2** – present as two distinct conformers of **L2** in *cis* arrangement – and two molecules of CH_3CN occupying the apical positions of the octahedral geometry. Due to the solvent mixture used during crystallization, these apical ligands are disordered with acetone in an occupancy ratio of 0.35 : 0.65(3), respectively. Again, the CH_3CN co-ligand coordinates *via* its N-atom (N9–Fe1 2.095(7) Å) and deviates from the ideal position on the apical axis (Fe1–N9–C33 160.7(6)°). The two conformers of **L2** differ in the position of the tz moiety relative to the anthracene plane (torsion angle: 23.5(10)° *vs.* 36.8(12)°, for both the tetrazolic C-atoms are orientated towards the anthracene plane). The distance of the coordinating tetrazolic *N*4-atom of these conformers is slightly different: 2.127(6) Å (N4–Fe1) *vs.* 2.140(6) Å (N8–Fe1). Like in **2**, the connection to the neighboring Fe(II)-atoms is realized by the bridging coordination mode of **L2**, with Fe–Fe distances of 14.8929(15) Å and 15.1700(16) Å.

For both CPs (**2** and **3**), two non-coordinating anions (ClO_4^-) and two molecules of CH_3CN are embedded in the crystal lattice per Fe-atom (Fig. S43 and S48).

According to XRPD, the bulk powders of the coordination compounds **1–3** are single-phase. In **3**, partial axial co-ligand exchange during crystallization does not seem to affect the structure of the coordination polymer, as evidenced by the good agreement between the experimental XRPD pattern – where no co-ligand disorder is present, as no acetone is used during synthesis – and the reflections calculated from the SC data.

The analytical data of bulk samples in solid state for the ligands **L1** and **L2** (ATR-IR, UV-Vis and PL) as well as for the coordination compounds **1–3** (ATR-IR, UV-Vis, PL, magnetic susceptibility measurements) discussed in the following chapters are shown in the SI.

Magnetic measurements

The magnetic moments of the bulk powder material of **1–3** (Fig. 6) were measured in cooling mode from 300 K to 10 K and subsequently in heating mode from 10 K to 380 K under an applied magnetic field of 1 T in steps of 10 K min^{-1} (settle mode). For **1**, the value of the magnetic susceptibility-temperature product ($\chi_M T$) was found to be 3.46 cm^3 K mol^{-1} above 300 K, which is a typically observed value for an Fe(II) ion in the HS state with apparent orbital contribution (S = 2; g = 2.2; $\chi_M T$ = 3.6 cm^3 K mol^{-1}).[71,72] Starting at 300 K, $\chi_M T$ gradually decreases until a value of 2.42 cm^3 K mol^{-1} at 30 K, showing an incomplete spin transition with approximately 70% of the Fe(II) ions remaining in HS state. The steep decrease after 30 K can be attributed to zero field splitting.[73]

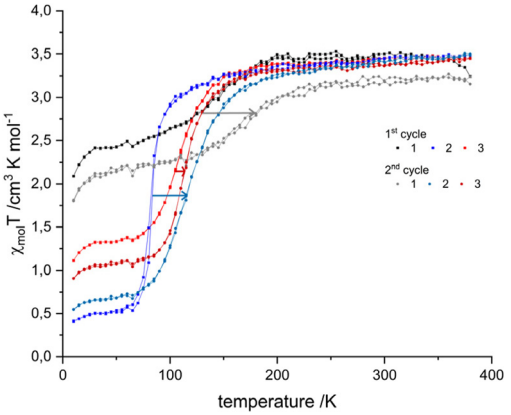

Fig. 6 Temperature-dependent magnetic susceptibility measurements for **1** (black), **2** (blue) and **3** (red). The change between the first and second cycle is pointed out with arrows in the respective color chosen for each compound.

Compound **2** shows a similar initial $\chi_M T$ value of 3.45 cm^3 K mol^{-1} for the HS state of Fe(II), which gradually decreases to 2.96 cm^3 K mol^{-1} from 300 K to 105 K. A subsequent steep decrease of $\chi_M T$ to 0.55 cm^3 K mol^{-1} at 55 K was observed, which was again followed by a gradual decrease to 0.50 cm^3 K mol^{-1} at 30 K. For **2**, a spin transition temperature of $T_{1/2}$ = 85 K was determined as the temperature at which the first derivative of $\chi_M T$ with respect to T ($\delta(\chi_M T)/\delta T$) reaches its maximum. The amount of Fe(II) ions in HS is 15%.

The connection of SCO centers through dimerized anthracene units in CP **2**, leads to greater rigidity and facilitates a more efficient propagation of volume changes associated with the spin transition throughout the lattice and therefore increases abruptness of the transition, compared to **1**.[74]

The SCO of compound **3** is gradual with a determined $T_{1/2}$ of 105 K, at 30 K 38% of the Fe(II) ions are left in HS state. The smaller amount of Fe(II) ions in HS at low temperatures in **2** compared to **3** can be explained by a less uniform propagation of the spin transition in the 2D CP due to different Fe–N distances (*vide supra*) and stabilization of the LS state.[75] The HS fractions remaining at 10 K are likely due to topological or structural irregularities resulting in a probable "hidden" two-step transition, only fully investigable by cooling down further, below 10 K (ref. 76) or a result of slow relaxation processes which would explain the relatively low transition temperatures

as well.[77,78] Since the cooling and heating curves are overlapping, the event of thermal hysteresis can be excluded in all three compounds.

Moreover, SC data reveal HS state distances for **3** at 100 K (*vide supra*), which contrast with the results from magnetic measurements. This difference likely arises because magnetic data reflect the combined thermal response of many particles, whereas structural data capture the transition in a single SC. The structural transition is therefore often sharper than the magnetic one.[79] Additionally, it has to be noted that the disordered acetone in the SC data of **3**, a result from the SC synthesis, implies the presence of two structurally identical but magnetically different behaving species which may depress the spin transition temperature below 100 K.[80]

To investigate a potential effect on the magnetic behavior due to crystal solvate loss (according to the results of thermal analysis – *vide infra*), a second heating and cooling cycle was performed. The general trend of a shift of $T_{1/2}$ to higher temperatures in the second cycle was observed.

For **1**, the starting value of $\chi_M T$ is 3.15 cm^3 K mol^{-1}, reduced by 10% compared to the original value. It can be assumed that the loss of acetonitrile causes irreversible degradation of the material.[81]

For **2**, the second cycle reveals a curve showing a more gradual SCO. The spin transition temperature was found to have increased to 115 K. Additionally, the amount of remaining Fe(II) ions in HS at 30 K is 2% higher after a prior cycle. In contrast to **2**, the second cycle of **3** results in a more abrupt SCO than the first one. The spin transition temperature is shifted to a higher temperature as well, namely to 110 K. Furthermore, more Fe(II) ions (70%) are now switched to the LS state. For the two latter compounds the loss of crystal solvate affects the packing and thus presumably the intermolecular interactions which lead to an increase of the spin transition temperature.[82,83] Neither **2** nor **3** are as altered as compound **1**, the complete amount of Fe(II) ions returns into the HS state. The higher amount of Fe(II) ions still in HS for the second cycle in **2** can be ascribed to a decreased cooperativity due to Fe(II) centers with varying surroundings considering the continuous crystal solvate loss over a broader temperature range according to the thermal analysis (*vide infra*).[80]

Photophysical measurements

The [4 + 4] photocycloaddition of **L1** to **L2** results in several changes in the IR spectra. The $\nu_{CH(tz)}$ band shifts from 3137 cm^{-1} in **L1** to 3162 cm^{-1} in **L2**, due to disruption in the aromaticity of the neighboring anthracene rings. This disruption also results in spectral changes in the region from 3120–3000 cm^{-1}, because of conversion of aromatic into aliphatic C–H stretching vibrations. The new intense bands at 785 cm^{-1}, 677 cm^{-1} and 639 cm^{-1} can be ascribed to specific vibrations (C–H out of plane bending and ring deformations) of the cyclobutane ring in **L2**.[37,64,84]

As described for other tz ligands the $\nu_{CH(tz)}$ band shifts upon coordination,[85] in the case of **1** the $\nu_{CH(tz)}$ band shifts from 3137 cm^{-1} in **L1** to 3159 cm^{-1} in **1**. The degenerated asymmetric bending mode of the non-coordinating anion appears as very intense band at 622 cm^{-1}. In addition, the symmetric stretching mode of the ClO_4^- anion is visible as band at 458 cm^{-1} with very low intensity.[86,87] The ν_{CN} band of the co-ligand is observable at 2277 cm^{-1}. Coordination compound **2** shows very similar IR characteristics as coordination compound **1**. The $\nu_{CH(tz)}$ band shifts even more to 3164 cm^{-1}, this is due to the fact that now also the shift of the $\nu_{CH(tz)}$ band of **L2** contributes. The characteristic bands for the anion and the co-ligand show only small shifts from **1** to **2** of a few wavenumbers and will therefore not be discussed in detail. **2** exhibits also the characteristic bands of the cyclobutane ring of **L2** with slight shifts to 782 cm^{-1} (loss of intensity), 681 cm^{-1} and 640 cm^{-1}. **3** exhibits a $\nu_{CH(tz)}$ band shift from 3162 cm^{-1} in **L2** to 3167 cm^{-1} and also shows characteristic bands of the co-ligand (2299 cm^{-1}) and the anion (623 cm^{-1}). The characteristic bands of the cyclobutane ring shift between 1 cm^{-1} and 5 cm^{-1} to higher wavenumbers.

The solid-state UV-Vis spectra of **L1** exhibits a steep increase in absorption from 200 nm to 250 nm. Above 250 nm, the increase is only weak until at approx. 420 nm the absorption falls to a low level without any specific features. This broad band can be ascribed to the π–π* transition of anthracene.[36] Ligand **L2** exhibits two intense absorption bands with maxima at 240 nm and 276 nm. The anthracene specific absorption between 350 nm and 400 nm is lost in **L2**,[59] where only an absorption plateau at low intensity is visible. In summary, **L1** shows high absorption between approx. 300 nm and 420 nm, whereas **L2** shows high absorption at higher energies (between 210 nm and 300 nm). Coordination compound **1** exhibits a similar spectrum to **L1** with an additional band at 234 nm. **2** features the absorption behavior of **L1** and **L2** with broad and intense band at 264 nm and high absorption levels between 300 nm and 400 nm. When comparing CP **3** to the uncoordinated ligand **L2** there are no additional features to be reported (Fig. S2).

A broad band centered at 870 nm can be found for **1**–**3** (Fig. S1), corresponding to the $^5T_2 \rightarrow {}^5E$ transition in Fe(II) which is characteristic for the HS state.[88]

Fig. S3 shows the solid-state emission spectra obtained upon excitation at 390 nm for **L1** and **1** and at 370 nm for **L2**, **2** and **3**. **L1** exhibits a broad featureless emission spectrum with an emission intensity maximum (λ_{max}) at 457 nm. The position of λ_{max} is consistent with literature reports on other anthracene derivatives with a similar arrangement of the anthracene units.[89] After photocycloaddition, the resulting **L2** displays a distinct emission spectrum featuring three maxima at 400 nm, 420 nm, 445 nm. This spectral pattern, attributed to a series of vibrational modes associated with the π*–π transition in dianthracene is in agreement with previous studies.[36] Additionally, **L2** exhibits a shoulder peak around 470 nm on the lower energy side of the main features, followed by a weak, gradually diminishing emission beyond 495 nm.

In the mononuclear complex **1**, interactions between **L1** and the Fe(II) center induce a hypsochromic shift of 27 nm, resulting in a new λ_{max} of 430 nm for **1**, which is in accordance with literature observations for a similar system.[30]

In the case of the 1D CP **2** (bearing both ligands **L1** and **L2**), λ_{max} is present at 428 nm, a shoulder peak at 448 nm and a weakly pronounced feature at 480 nm are observed in the emission spectrum. By contrast, in the 2D CP **3** (which contains only **L2**), the coordinated ligand retains the spectral characteristics of uncoordinated **L2**, showing only negligible wavelength shifts of the three maxima. This indicates that the coordination induces minimal energetic perturbation in **L2**.

Alternative excitation at 276 nm results in different, less intense emission spectra for **L2** and **3** with λ_{max} at 449 and 459 nm, respectively, a behavior that has also been reported by other groups (Fig. S4).[28]

Variable temperature emission spectra were recorded in 10 K steps between 77 K–298 K in order to reveal a potential synergistic interplay between SCO and PL. The position of the peak (λ_{max}) and the integrated intensity were extracted by fitting the temperature dependent PL data using multiple Gaussian functions.[79,90]

The main emission maximum of **L1** steadily declines in PL intensity as temperature increases due to thermal quenching and this reduction is accompanied by a redshift of λ_{max} (Fig. S5). The temperature dependent PL changes of **L1** resemble those of a previously reported anthracene triazole derivative.[30] Analysis of the spectra for **L1** was performed by fitting with two Gaussian functions over the whole temperature range, details of the thermal peak evolution are shown in Fig. S6 and S7.

In **L2**, highest emission intensity is also observed at the lowest temperature, which steadily decreases with increasing temperature and can also be ascribed to thermal quenching. The λ_{max} positions remain almost unchanged over the investigated temperature range for all fitted peaks. In the temperature range of 157 K–187 K a notable decline in the integrated intensity was observed (Fig. S9), for which no conclusive explanation has been found so far.

The mononuclear complex **1** also exhibits highest emission intensity at the lowest temperature. Both, λ_{max} of the absolute maximum and the shoulder peak show a continuous hypsochromic shift with increasing temperature (Fig. S11). However, peak deconvolution with Gaussian functions does not show any clear trend or remarkable features in the integrated peak intensity, which could be attributed to a coupling with the spin transition (Fig. S12 and S13). Even if the prerequisites for luminescence modulation (*i.e.*, *via* structural or electronic synergy) are met, the number of LS centers might simply be too low, and the spin transition too gradual, to induce a measurable luminescence modulation.

The PL spectrum of **2** shows a complex peak structure at 77 K which can be fitted by using five Gaussian functions (Fig. 7a). The evolution of the integrated peak intensities is demonstrated in Fig. 7b and S16, which reveals a significant increase from 77 K until 107 K for peak 1–3. The integrated intensity of peak 2 further rises slightly until 117 K, before a decline can be observed. Peak 3 disappears at temperatures above 137 K, which, leads to the abrupt increase in the integrated intensity for peak 2.

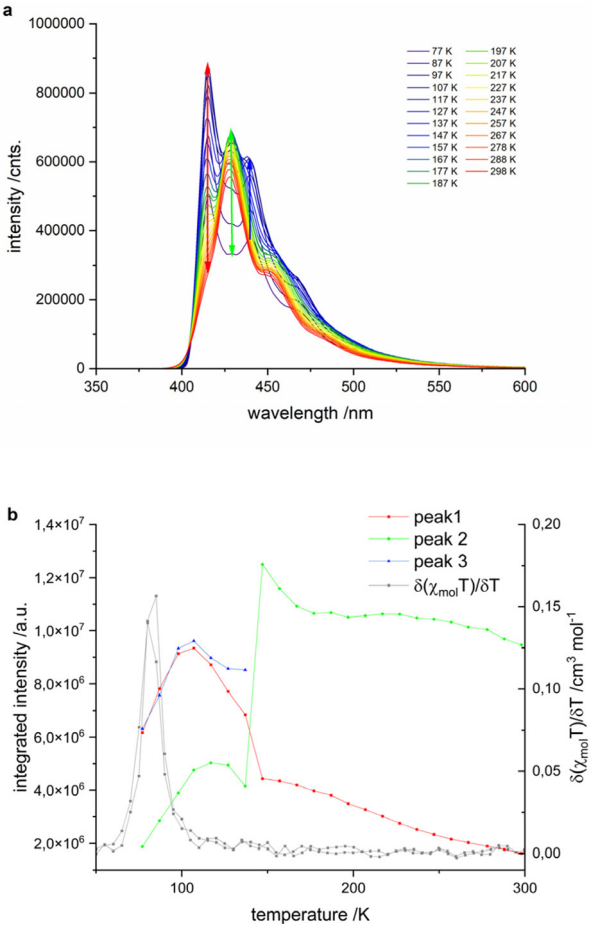

Fig. 7 (a) Temperature-dependent fluorescence emission spectra of **2**. $\lambda_{exc.}$ = 370 nm. Colored arrows indicate the evolution of the respective fitted peaks with increasing temperature (red: peak 1; green: peak 2; blue: peak 3). (b) Temperature dependance of the integrated intensity of the fitted peaks 1, 2 and 3 along with the derivative of the magnetic susceptibility for **2** of the first cooling-heating cycle.

Declining integrated intensity at temperatures above 107 K for peak 1 and 3 and above 117 K for peak 2 can be again ascribed to thermal quenching effects.

The magnetic susceptibility, shown as $\delta(\chi_M T)/\delta T$ in Fig. 7b, exhibits a $T_{1/2}$ of approximately 85 K (*vide supra*), which is about 20 K lower than the temperature at which significant changes in PL properties occur. Nevertheless, we propose a synergistic interaction between spin transition and PL modulation. The observed deviations of approximately 20 K fall within the literature reported range and can be attributed to differences in the instrumental setup (*i.e.* sample chamber, heating/cooling rates) used for magnetic and PL measurements.[47]

In contrast to the ligand **L2**, the 2D coordination compound **3** does not show the highest emission intensity at the lowest temperature (77 K). However, apart from intensity changes, the spectra at low temperature are very similar to both the rt spectrum of **3** and that of **L2** (Fig. S17). Consequently, peak fitting was performed analogously to **L2**, identifying five distinct

peaks (Fig. S19). Between 77 K and 147 K, the integrated intensity of the most pronounced peaks (1–3) increases, followed by a gradual decline until rt. Notably, as observed for **L2**, an undefined drop in integrated intensity occurs in the temperature range from 157–177 K.

The comparison of the temperature dependent PL measurements of **L2** and **3** shows that the fluorescence properties might be influenced by the spin state of Fe(II). Although the PL intensity increases as the LS state is depopulated and subsequently decreases in the HS state due to thermal quenching, this behavior does not exactly correlate with $\delta(\chi_M T)/\delta(T)$, as illustrated in Fig. 8. Similar to our observations in **2**, we still assume a spin state dependent fluorescence behavior. In that case, aside from instrument-related deviations, the spin transition in **3** appears more gradual than in **2**, further broadening the range of the synergistic response.

We suppose a distinct spectral overlap of the metal-to-ligand charge transfer (MLCT) band and/or the spin-allowed d–d transitions ($^1A_1 \rightarrow {}^1T_1$, $^1A_1 \rightarrow {}^1T_2$) of Fe(II) in the range of 400–800 nm (ref. 91 and 92) with the emission band of the coordination compounds **2** and **3**. This allows for a spin s selective fluorescence quenching *via* an energy transfer from the ligand to Fe(II) ions in LS state. Upon the thermally induced transition to the HS state, the MLCT band may weaken/shift,[93] and the d–d transition ($^5T_2 \rightarrow {}^5E$) undergoes a bathochromic shift to around 870 nm, diminishing the spectral overlap and consequently enhancing fluorescence intensity as shown in Fig. S20 and S21.[19,28,30,51,94] At this stage we cannot draw definitive conclusions about the mechanistic coupling between the SCO and PL.

Remarkably, in compound **2**, not only does the emission intensity change, but the overall emission profile varies drastically with increasing temperature, concomitant with the spin transition. This suggests that peaks have a different electronic origin and/or structural rearrangements of the anthracene units occur due to accompanying unit cell volume changes upon spin transition.[23]

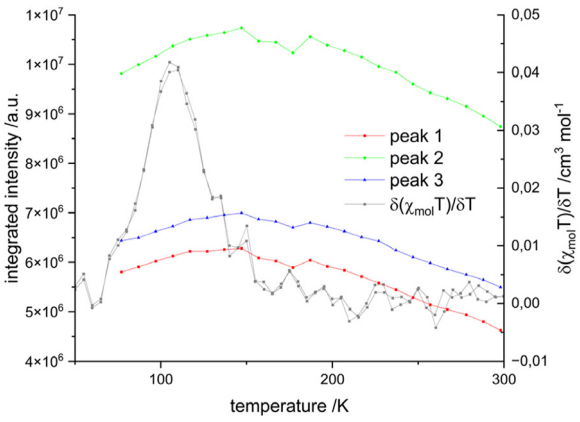

Fig. 8 Temperature dependence of the integrated intensity of the fitted peaks 1, 2 and 3 along with the derivative of the magnetic susceptibility for **3** of the first cooling-heating cycle.

Thermal analysis

The thermal analysis was performed using a heating rate of 5 °C min^{-1} from 25 to 210 °C under a nitrogen atmosphere (Fig. S23–S25). The TGA curve of **1** shows a continuous mass loss of approx. 3% in a temperature range from 25 to 90 °C. The second continuous mass loss of comparable magnitude takes place between 90 and 132 °C. A mass of approx. 3% is consistent with the mass of one CH_3CN crystal solvate molecule (2.8%) relative to the total molar mass of the coordination compound (1460.2 $gmol^{-1}$). Compound **2** shows a continuous release of two CH_3CN molecules until 140 °C. **3** reaches a lower plateau after the release of one CH_3CN molecule at 105 °C. In the temperature range of 131–210 °C, all TGA curves show a pronounced mass loss of approximately 11–13%, which closely matches the mass fraction of perchlorate present in the coordination compound. In the corresponding DSC curves, for all three compounds an exothermic event takes place around 154–161 °C, exhibiting a heat flow of 3–4 $mWmg^{-1}$. The exothermic event, together with the visual observation of a black foam emerging from the pierced DSC crucible, provides strong evidence for combustion of the CP initiated by the perchlorate anion. The DSC curve of **3** shows another exothermic event above 200 °C with an accompanying mass loss of about 2%.

Conclusions

In this work, we report the successful synthesis of a novel 1*H*-tetrazole ligand **L1** bearing a fluorescent anthracene moiety and further demonstrate its efficient [4 + 4] photocycloaddition upon light irradiation to form **L2**, as well as its monomerization back to **L1** upon heating.

Utilizing **L1**, we synthesized a heteroleptic mononuclear Fe(II) complex **1**, whose outstanding [4 + 4] photocycloaddition increased the dimensionality to yield the 1D CP **2**. Remarkably, this solid-state photodimerization is even achievable in a SC-to-SC fashion, namely a topochemical reaction. Moreover, by employing the pre-dimerized ditopic anthracene ligand **L2**, we obtained the 2D CP **3**.

The increased dimensionality (realized by dimerization of the anthracene units) enhanced the cooperativity of the SCO, resulting in more abrupt and complete spin transitions for the CPs **2** and **3**. A distinct coupling between SCO and PL properties was observed. These findings suggest that electronic coupling, accompanied by structural changes during the spin transition, leads to PL modulation; however, detailed mechanistic insights *via* DFT calculations are still pending. Additionally, investigations of the relaxation processes by *i.e.* varying the scan rates during the magnetic measurements would give more insight into the reason for the low transition temperatures and the population of the HS state at low temperatures.

From an applicational perspective, the SCO-PL interplay holds great promise for nanoscale sensing, where PL readouts can overcome limitations of weak magnetic signals. Moreover,

CPs offer the potential to create large single atomic layer surfaces, which is of interest for the development of thin film materials or nanoparticles. In this context, the ability of **L1** to undergo the [4 + 4] photocycloaddition even after complexation paves the way for functional surface coatings with SCO materials *e.g.*, by covalently grafting **1** onto surface hosting anthracene moieties *via* irradiation.

Our results establish anthracene dimers as effective bridging ligands in luminescent SCO CPs, providing a robust platform for further exploration and optimization.

Future studies, which include systematic variations of the co-ligand (various nitriles) and counterions (*i.e.*, non-coordinating *vs.* coordinating anions) to tune the spin transition of the system are in progress. Moreover, structural characterizations *via* SC-XRD in the LS state (<80 K) are to be conducted.

Conflicts of interest

There are no conflicts to declare.

Data availability

The data supporting this article have been included as part of the supplementary information (SI). Supplementary information: experimental protocols, spectroscopic and magnetic measurements, thermal analysis, crystal structures, XRPD, NMR and IR spectra. See DOI: **https://doi.org/10.1039/d5qi01281c**.

CCDC 2427600 (**1**), 2427601 (**2**), 2427602 (**L1-p1**), 2427603 (**L1-p2**), 2427604 (**L2-ns**), 2427605 (**L2-s1**) and 2427606 (**L2-s2**) contain the supplementary crystallographic data for this paper.[95a–g]

Acknowledgements

The authors thank Carola Haslinger (Polymer Chemistry and Technology, TU Wien) for her support and for providing access to the LED equipment, as well as Werner Artner (X-ray Center, TU Wien) for his assistance. Furthermore, we express our gratitude to Dominik Eder and Alexey Cherevan (Institute of Materials Chemistry, TU Wien) for granting permission to use their FluoTime 300 fluorescence lifetime spectrometer. For open access purposes, P. Weinberger has applied a CC BY public copyright license to any author accepted manuscript version arising from this submission.

References

1 L. Cambi and L. Szegö, The magnetic susceptibility of complex compounds, *Ber. Dtsch. Chem. Ges.*, 1931, **64**, 2591–2598.
2 H. J. Shepherd, C. Bartual-Murgui, G. Molnár, J. A. Real, M. C. Muñoz, L. Salmon and A. Bousseksou, Thermal and pressure-induced spin crossover in a novel three-dimensional Hoffman-like clathrate complex, *New J. Chem.*, 2011, **35**, 1205–1210.
3 M. C. Muñoz and J. A. Real, Thermo-, piezo-, photo- and chemo-switchable spin crossover iron(II)-metallocyanate based coordination polymers, *Coord. Chem. Rev.*, 2011, **255**, 2068–2093.
4 M. L. Boillot, S. Pillet, A. Tissot, E. Riviere, N. Claiser and C. Lecomte, Ligand-driven light-induced spin change activity and bidirectional photomagnetism of styrylpyridine iron(II) complexes in polymeric media, *Inorg. Chem.*, 2009, **48**, 4729–4736.
5 P. Gütlich, A. B. Gaspar and Y. Garcia, Spin state switching in iron coordination compounds, *Beilstein J. Org. Chem.*, 2013, **9**, 342–391.
6 P. Gütlich, Spin Crossover – Quo Vadis?, *Eur. J. Inorg. Chem.*, 2013, 581–591.
7 M. A. Halcrow, *Spin–Crossover Materials: Properties and Applications*, John Wiley & Sons, Chichester, 2013.
8 P. G. Lacroix, I. Malfant, J. A. Real and V. Rodriguez, From Magnetic to Nonlinear Optical Switches in Spin-Crossover Complexes, *Eur. J. Inorg. Chem.*, 2013, **2013**, 615–627.
9 M. Wang, Z. Y. Li, R. Ishikawa and M. Yamashita, Spin crossover and valence tautomerism conductors, *Coord. Chem. Rev.*, 2021, **435**, 213819.
10 I. A. Gural'skiy, V. A. Reshetnikov, A. Szebesczyk, E. Gumienna-Kontecka, A. I. Marynin, S. I. Shylin, V. Ksenofontov and I. O. Fritsky, Chiral spin crossover nanoparticles and gels with switchable circular dichroism, *J. Mater. Chem. C*, 2015, **3**, 4737–4741.
11 H. J. Shepherd, C. M. Quintero, G. Molnár, L. Salmon and A. Bousseksou, *Spin–Crossover Materials*, 2013, 347–373.
12 M. K. Javed, A. Sulaiman, M. Yamashita and Z. Y. Li, Shedding light on bifunctional luminescent spin crossover materials, *Coord. Chem. Rev.*, 2022, **467**, 214594.
13 K. Sun, J. P. Xue, Z. S. Yao and J. Tao, Synergistic strategies for the synthesis of Fe(II)-based bifunctional fluorescent spin-crossover materials, *Dalton Trans.*, 2022, **51**, 16044–16054.
14 Z. P. Ni, J. L. Liu, N. Hogue, W. Liu, J. Y. Li, Y. C. Chen and M. L. Tong, Recent advances in guest effects on spin-crossover behavior in Hofmann-type metal-organic frameworks, *Coord. Chem. Rev.*, 2017, **335**, 28–43.
15 K. Senthil Kumar and M. Ruben, Emerging trends in spin crossover (SCO) based functional materials and devices, *Coord. Chem. Rev.*, 2017, **346**, 176–205.
16 A. B. Gaspar, V. Ksenofontov, M. Seredyuk and P. Gütlich, Multifunctionality in spin crossover materials, *Coord. Chem. Rev.*, 2005, **249**, 2661–2676.
17 M. Matsuda, H. Isozaki and H. Tajima, Reproducible on-off switching of the light emission from the electroluminescent device containing a spin crossover complex, *Thin Solid Films*, 2008, **517**, 1465–1467.
18 M. Engeser, L. Fabbrizzi, M. Licchelli and D. Sacchi, A fluorescent molecular thermometer based on the nickel(II) high-spin/low-spin interconversion, *Chem. Commun.*, 1999, 1191–1192.

19 L. Salmon, G. Molnár, D. Zitouni, C. Quintero, C. Bergaud, J. C. Micheau and A. Bousseksou, A novel approach for fluorescent thermometry and thermal imaging purposes using spin crossover nanoparticles, *J. Mater. Chem.*, 2010, **20**, 5499–5503.
20 C. Bartual-Murgui, A. Akou, C. Thibault, G. Molnár, C. Vieu, L. Salmon and A. Bousseksou, Spin-crossover metal-organic frameworks: promising materials for designing gas sensors, *J. Mater. Chem. C*, 2015, **3**, 1277–1285.
21 Z. Hu, B. J. Deibert and J. Li, Luminescent metal-organic frameworks for chemical sensing and explosive detection, *Chem. Soc. Rev.*, 2014, **43**, 5815–5840.
22 C. Lochenie, K. Schötz, F. Panzer, H. Kurz, B. Maier, F. Puchtler, S. Agarwal, A. Kohler and B. Weber, Spin-Crossover Iron(II) Coordination Polymer with Fluorescent Properties: Correlation between Emission Properties and Spin State, *J. Am. Chem. Soc.*, 2018, **140**, 700–709.
23 I. Suleimanov, O. Kraieva, J. S. Costa, I. O. Fritsky, G. Molnár, L. Salmon and A. Bousseksou, Electronic communication between fluorescent pyrene excimers and spin crossover complexes in nanocomposite particles, *J. Mater. Chem. C*, 2015, **3**, 5026–5032.
24 S. Gharbi, H. Zrida, K. Hriz, M. Chemek, N. Wazzan and M. Majdoub, Synthesis of new Tetrazole based-semiconducting polymers for optoelectronic application: Study of the effect of anthracene group on photophysical properties, *J. Mol. Struct.*, 2022, **1250**, 131760.
25 Y. H. Kim, H. C. Jeong, S. H. Kim, K. Yang and S. K. Kwon, High–Purity–Blue and High–Efficiency Electroluminescent Devices Based on Anthracene, *Adv. Funct. Mater.*, 2005, **15**, 1799–1805.
26 M. S. Kahouech, K. Hriz, S. Touaiti and J. Bassem, New anthracene-based-phtalocyanine semi-conducting materials: Synthesis and optoelectronic properties, *Mater. Res. Bull.*, 2016, **75**, 144–154.
27 R. Turo-Cortés, M. Meneses-Sánchez, T. Delgado, C. Bartual-Murgui, M. C. Muñoz and J. A. Real, Coexistence of luminescence and spin-crossover in 2D iron(II) Hofmann clathrates modulated through guest encapsulation, *J. Mater. Chem. C*, 2022, **10**, 10686–10698.
28 M. Meneses-Sánchez, L. Piñeiro-López, T. Delgado, C. Bartual-Murgui, M. C. Muñoz, P. Chakraborty and J. A. Real, Extrinsic vs. intrinsic luminescence and their interplay with spin crossover in 3D Hofmann-type coordination polymers, *J. Mater. Chem. C*, 2020, **8**, 1623–1633.
29 P. Dierks, A. Papcke, O. S. Bokareva, B. Altenburger, T. Reuter, K. Heinze, O. Kuhn, S. Lochbrunner and M. Bauer, Ground- and Excited-State Properties of Iron(II) Complexes Linked to Organic Chromophores, *Inorg. Chem.*, 2020, **59**, 14746–14761.
30 C. F. Wang, G. Y. Yang, Z. S. Yao and J. Tao, Monitoring the Spin States of Ferrous Ions by Fluorescence Spectroscopy in Spin-Crossover-Fluorescent Hybrid Materials, *Chem. – Eur. J.*, 2018, **24**, 3218–3224.
31 H. Matsukizono, K. Kuroiwa and N. Kimizuka, Self-assembly-directed Spin Conversion of Iron(II) 1,2,4-Triazole Complexes in Solution and Their Effect on Photorelaxation Processes of Fluorescent Counter Ions, *Chem. Lett.*, 2008, **37**, 446–447.
32 G. M. J. Schmidt, Photodimerization in the solid state, *Pure Appl. Chem.*, 1971, **27**, 647–678.
33 M. D. Cohen, G. M. J. Schmidt and F. I. Sonntag, Topochemistry. Part II. The photochemistry of trans-cinnamic acids, *J. Chem. Soc.*, 1964, **384**, 2000–2013.
34 K. Hema, A. Ravi, C. Raju, J. R. Pathan, R. Rai and K. M. Sureshan, Topochemical polymerizations for the solid-state synthesis of organic polymers, *Chem. Soc. Rev.*, 2021, **50**, 4062–4099.
35 C. Raju, G. R. Ramteke, K. V. J. Jose and K. M. Sureshan, Cascading Effect of Large Molecular Motion in Crystals: A Topotactic Polymorphic Transition Paves the Way to Topochemical Polymerization, *J. Am. Chem. Soc.*, 2023, **145**, 9607–9616.
36 X. D. Huang, Y. Xu, K. Fan, S. S. Bao, M. Kurmoo and L. M. Zheng, Reversible SC-SC Transformation involving [4 + 4] Cycloaddition of Anthracene: A Single-Ion to Single-Molecule Magnet and Yellow-Green to Blue-White Emission, *Angew. Chem., Int. Ed.*, 2018, **57**, 8577–8581.
37 Y. Chen, C. Yu, X. Zhu and Q. Yu, Photomechanical effects based on a one-dimensional Zn coordination polymer crystal driven by [4 + 4] cycloaddition, *Dalton Trans.*, 2023, **52**, 12194–12197.
38 M. Castellano, J. Ferrando-Soria, E. Pardo, M. Julve, F. Lloret, C. Mathoniere, J. Pasan, C. Ruiz-Perez, L. Canadillas-Delgado, R. Ruiz-Garcia and J. Cano, Photoswitching of the antiferromagnetic coupling in an oxamato-based dicopper(II) anthracenophane, *Chem. Commun.*, 2011, **47**, 11035–11037.
39 F. Spinelli, S. d'Agostino, P. Taddei, C. D. Jones, J. W. Steed and F. Grepioni, Activating [4 + 4] photoreactivity in the solid-state via complexation: from 9-(methylaminomethyl) anthracene to its silver(I) complexes, *Dalton Trans.*, 2018, **47**, 5725–5733.
40 X. D. Huang, M. Kurmoo, S. S. Bao, K. Fan, Y. Xu, Z. B. Hu and L. M. Zheng, Coupling photo-, mechano- and thermochromism and single-ion-magnetism of two mononuclear dysprosium-anthracene-phosphonate complexes, *Chem. Commun.*, 2018, **54**, 3278–3281.
41 S. E. Qiu and S. Y. Yang, Reversible photo/thermal solid-state transformation of a coordination polymer, *CrystEngComm*, 2020, **22**, 6339–6346.
42 M. Garai and K. Biradha, Coordination polymers of organic polymers synthesized via photopolymerization of single crystals: two-dimensional hydrogen bonding layers with amazing shock absorbing nature, *Chem. Commun.*, 2014, **50**, 3568–3570.
43 M. G. Reeves, E. Tailleur, P. A. Wood, M. Marchivie, G. Chastanet, P. Guionneau and S. Parsons, Mapping the cooperativity pathways in spin crossover complexes, *Chem. Sci.*, 2020, **12**, 1007–1015.
44 R. Ohtani and S. Hayami, Guest-Dependent Spin-Transition Behavior of Porous Coordination Polymers, *Chem. – Eur. J.*, 2017, **23**, 2236–2248.

45 N. F. Sciortino and S. M. Neville, Two-Dimensional Coordination Polymers with Spin Crossover Functionality, *Aust. J. Chem.*, 2014, **67**, 1553–1562.
46 C.-F. Wang, R.-F. Li, X.-Y. Chen, R.-J. Wei, L.-S. Zheng and J. Tao, Synergetic spin crossover and fluorescence in one-dimensional hybrid complexes, *Angew. Chem., Int. Ed.*, 2015, **54**, 1574–1577.
47 I. F. Diaz-Ortega, E. L. Fernandez-Barbosa, S. Titos-Padilla, S. J. A. Pope, J. R. Jimenez, E. Colacio and J. M. Herrera, Monitoring spin-crossover phenomena via Re(I) luminescence in hybrid Fe(II) silica coated nanoparticles, *Dalton Trans.*, 2021, **50**, 16176–16184.
48 I. Suleimanov, G. Molnár, L. Salmon and A. Bousseksou, Near-Infrared Luminescence Switching in a Spin-Crossover Polymer Nanocomposite, *Eur. J. Inorg. Chem.*, 2017, 3446–3451.
49 I. Suleimanov, O. Kraieva, G. Molnár, L. Salmon and A. Bousseksou, Enhanced luminescence stability with a Tb-spin crossover nanocomposite for spin state monitoring, *Chem. Commun.*, 2015, **51**, 15098–15101.
50 J. M. Herrera, S. Titos-Padilla, S. J. A. Pope, I. Berlanga, F. Zamora, J. J. Delgado, K. V. Kamenev, X. Wang, A. Prescimone, E. K. Brechin and E. Colacio, Studies on bifunctional Fe(II)-triazole spin crossover nanoparticles: time-dependent luminescence, surface grafting and the effect of a silica shell and hydrostatic pressure on the magnetic properties, *J. Mater. Chem. C*, 2015, **3**, 7819–7829.
51 S. Titos-Padilla, J. M. Herrera, X. W. Chen, J. J. Delgado and E. Colacio, Bifunctional hybrid SiO_2 nanoparticles showing synergy between core spin crossover and shell luminescence properties, *Angew. Chem., Int. Ed.*, 2011, **50**, 3290–3293.
52 W. Zeni, M. Seifried, C. Knoll, J. M. Welch, G. Giester, B. Stöger, W. Artner, M. Reissner, D. Müller and P. Weinberger, Bifunctional Fe(II) spin crossover-complexes based on omega-(1H-tetrazol-1-yl) carboxylic acids, *Dalton Trans.*, 2020, **49**, 17183–17193.
53 C. Knoll, D. Muller, M. Seifried, G. Giester, J. M. Welch, W. Artner, K. Hradil, M. Reissner and P. Weinberger, Cooperativity in spin crossover materials as ligand's responsibility - investigations of the Fe(ii) - 1,3-bis((1H-tetrazol-1-yl)methyl)bicyclo[1.1.1]pentane system, *Dalton Trans.*, 2018, **47**, 5553–5557.
54 D. Muller, C. Knoll, M. Seifried, J. M. Welch, G. Giester, M. Reissner and P. Weinberger, Halogenated Alkyltetrazoles for the Rational Design of Fe(II) Spin-Crossover Materials: Fine-Tuning of the Ligand Size, *Chem. – Eur. J.*, 2018, **24**, 5271–5280.
55 D. Müller, C. Knoll, M. Seifried and P. Weinberger, ATR or transmission—A variable temperature study comparing both techniques using $[Fe(3ditz)_3](BF_4)_2$ as model system, *Vib. Spectrosc.*, 2016, **86**, 198–205.
56 J. Singh, N. Steck, D. De, A. Hofer, A. Ripp, I. Captain, M. Keller, P. A. Wender, R. Bhandari and H. J. Jessen, A Phosphoramidite Analogue of Cyclotriphosphate Enables Iterative Polyphosphorylations, *Angew. Chem., Int. Ed.*, 2019, **58**, 3928–3933.
57 T. Kamiya and Y. Saito, *Germany Pat.*, DEP21470235, 1971.
58 M. D. Cohen, The Photochemistry of Organic Solids, *Angew. Chem., Int. Ed. Engl.*, 1975, **14**, 386–393.
59 F. Cicogna, G. Ingrosso, F. Lodato, F. Marchetti and M. Zandomeneghi, 9-Anthroylacetone and its photodimer, *Tetrahedron*, 2004, **60**, 11959–11968.
60 H. G. Brittain, Polymorphism and solvatomorphism 2010, *J. Pharm. Sci.*, 2012, **101**, 464–484.
61 H. D. Becker, V. Langer and H. C. Becker, Photochemistry of 9-benzoylanthracene, *J. Org. Chem.*, 2002, **58**, 6394–6396.
62 M. Huber, M. Schöbinger, J. Cirera, B. Stöger and P. Weinberger, Design, Synthesis and Characterization of BODIPY based 1H-Tetrazole Ligands, *Eur. J. Org. Chem.*, 2025, e202401239.
63 T. Steiner, The hydrogen bond in the solid state, *Angew. Chem., Int. Ed.*, 2002, **41**, 49–76.
64 Q. Yu, X. Yang, Y. Chen, K. Yu, J. Gao, Z. Liu, P. Cheng, Z. Zhang, B. Aguila and S. Ma, Fabrication of Light-Triggered Soft Artificial Muscles via a Mixed-Matrix Membrane Strategy, *Angew. Chem., Int. Ed.*, 2018, **57**, 10192–10196.
65 A. Bialonska and R. Bronisz, High spin and spin-crossover two-dimensional coordination polymers containing Fe(II)(tetrazol-2-yl)4(solv)2 (solv = ethanol, acetonitrile) cores linked by flexible/elastic spacers, *Inorg. Chem.*, 2010, **49**, 4534–4542.
66 M. Huber, M. Schobinger, B. Stoger, M. Reissner and P. Weinberger, $T_{\frac{1}{2}}$ Tuning in a Synergistic BODIPY-Tetrazole Fe(II) Spin Crossover-Photoluminescence System via Counterion Variation, *Cryst. Growth Des.*, 2025, **25**, 8875–8885.
67 S. Ghosh, S. Kamilya, T. Pramanik, M. Rouzieres, R. Herchel, S. Mehta and A. Mondal, ON/OFF Photoswitching and Thermoinduced Spin Crossover with Cooperative Luminescence in a 2D Iron(II) Coordination Polymer, *Inorg. Chem.*, 2020, **59**, 13009–13013.
68 M. Quesada, F. Prins, E. Bill, H. Kooijman, P. Gamez, O. Roubeau, A. L. Spek, J. G. Haasnoot and J. Reedijk, Counterion effect on the spin-transition properties of the cation [Fe(btzx)3]2+ (btzx=m-Xylylenebis(tetrazole)), *Chem. – Eur. J.*, 2008, **14**, 8486–8499.
69 J. L. Wang, Q. Liu, X. J. Lv, R. L. Wang, C. Y. Duan and T. Liu, Magnetic fluorescent bifunctional spin-crossover complexes, *Dalton Trans.*, 2016, **45**, 18552–18558.
70 U. Müller and G. de la Flor, in *Symmetry Relationships between Crystal Structures: Applications of Crystallographic Group Theory in Crystal Chemistry*, Oxford University Press, 1st edn, 2013, ch. 16, pp. 217–224.
71 A. Benchohra, Y. Li, L. M. Chamoreau, B. Baptiste, E. Elkaim, N. Guillou, D. Kreher and R. Lescouezec, The Atypical Hysteresis of [Fe(C(6) F(5) Tp)(2)]: Overlay of Spin-Crossovers and Symmetry-Breaking Phase Transition, *Angew. Chem., Int. Ed.*, 2021, **60**, 8803–8807.
72 N. Hassan, P. Weinberger, F. Kubel, G. Molnar, A. Bousseksou, L. Dlhan, R. Boca and W. Linert, Two new

Fe(II) spin crossover complexes with tetrazol-1-yl-cycloalkane ligands, *Inorg. Chim. Acta*, 2009, **362**, 3629–3636.

73 H. Y. Wang, J. Y. Ge, C. Hua, C. Q. Jiao, Y. Wu, C. F. Leong, D. M. D'Alessandro, T. Liu and J. L. Zuo, Photo- and Electronically Switchable Spin-Crossover Iron(II) Metal-Organic Frameworks Based on a Tetrathiafulvalene Ligand, *Angew. Chem., Int. Ed.*, 2017, **56**, 5465–5470.

74 M. Quesada, H. Kooijman, P. Gamez, J. Sanchez Costa, P. J. van Koningsbruggen, P. Weinberger, M. Reissner, A. L. Spek, J. G. Haasnoot and J. Reedijk, $[Fe(\mu\text{-btzmp})_2(btzmp)_2](ClO_4)_2$: a doubly-bridged 1D spin-transition bistetrazole-based polymer showing thermal hysteresis behaviour, *Dalton Trans.*, 2007, 5434–5440.

75 C. M. Grunert, J. Schweifer, P. Weinberger, W. Linert, K. Mereiter, G. Hilscher, M. Muller, G. Wiesinger and P. J. van Koningsbruggen, Structure and physical properties of [μ-tris(1,4-bis(tetrazol-1-yl)butane-N4,N4′)iron(II)] bis (hexafluorophosphate), a new Fe(II) spin-crossover compound with a three-dimensional threefold interlocked crystal lattice, *Inorg. Chem.*, 2004, **43**, 155–165.

76 L. Zhang, G. C. Xu, H. B. Xu, V. Mereacre, Z. M. Wang, A. K. Powell and S. Gao, Synthesis, magnetic and photomagnetic study of new iron(II) spin-crossover complexes with N(4)O(2) coordination sphere, *Dalton Trans.*, 2010, **39**, 4856–4868.

77 A. Bousseksou, G. Molnar, L. Salmon and W. Nicolazzi, Molecular spin crossover phenomenon: recent achievements and prospects, *Chem. Soc. Rev.*, 2011, **40**, 3313–3335.

78 S. Schönfeld, C. Lochenie, P. Thoma and B. Weber, 1D iron(II) spin crossover coordination polymers with 3,3′-azopyridine – kinetic trapping effects and spin transition above room temperature, *CrystEngComm*, 2015, **17**, 5389–5395.

79 B. Benaicha, K. Van Do, A. Yangui, N. Pittala, A. Lusson, M. Sy, G. Bouchez, H. Fourati, C. J. Gomez-Garcia, S. Triki and K. Boukheddaden, Interplay between spin-crossover and luminescence in a multifunctional single crystal iron (II) complex: towards a new generation of molecular sensors, *Chem. Sci.*, 2019, **10**, 6791–6798.

80 T. Kosone, I. Tomori, C. Kanadani, T. Saito, T. Mochida and T. Kitazawa, Unprecedented three-step spin-crossover transition in new 2-dimensional coordination polymer Fe (II)(4-methylpyridine)(2)[Au(I)(CN)(2)](2), *Dalton Trans.*, 2010, **39**, 1719–1721.

81 Z.-Y. Li, Y.-Y. Wu, Y. Li, J.-H. Wang, A. Sulaiman, M. K. Javed, Y.-C. Zhang, W. Li and X.-H. Bu, Slow Phase Transition-Induced Scan Rate Dependence of Spin Crossover in a Two-Dimensional Supramolecular Fe(III) Complex, *CCS Chem.*, 2023, **5**, 412–422.

82 P. D. Southon, L. Liu, E. A. Fellows, D. J. Price, G. J. Halder, K. W. Chapman, B. Moubaraki, K. S. Murray, J. F. Letard and C. J. Kepert, Dynamic interplay between spin-crossover and host-guest function in a nanoporous metal-organic framework material, *J. Am. Chem. Soc.*, 2009, **131**, 10998–11009.

83 M. Huber, M. Schobinger, B. Stoger, M. Reissner and P. Weinberger, $T_{1/2}$ Tuning in a Synergistic BODIPY-Tetrazole Fe(II) Spin Crossover-Photoluminescence System via Counterion Variation, *Cryst. Growth Des.*, 2025, **25**, 8875–8885.

84 J. C. Liu, Q. Zou, X. D. Huang, S. S. Bao and L. M. Zheng, Dysprosium Coordination Polymer Incorporating Dianthracene: Thermo-induced Phase Transition Accompanied with Magnetic and Optical Changes, *Eur. J. Inorg. Chem.*, 2021, **2021**, 1565–1570.

85 M. Schöbinger, M. Huber, B. Stöger, C. Hametner and P. Weinberger, Structural tuning of tetrazole-BODIPY Ag(i) coordination compounds via co-ligand addition and counterion variation, *CrystEngComm*, 2025, **27**, 2689–2697.

86 H. Siebert, Kraftkonstante und Strukturchemie. V. Struktur der Sauerstoffsäuren, *Z. Anorg. Allg. Chem.*, 1954, **275**, 225–240.

87 D. L. Lewis, E. D. Estes and D. J. Hodgson, The infrared spectra of coordinated perchlorates, *J. Cryst. Mol. Struct.*, 1975, **5**, 67–74.

88 A. Hauser, Intersystem crossing in the [Fe(ptz)6](BF4)2 spin crossover system (ptz=1-propyltetrazole), *J. Chem. Phys.*, 1991, **94**, 2741–2748.

89 T. Hinoue, Y. Shigenoi, M. Sugino, Y. Mizobe, I. Hisaki, M. Miyata and N. Tohnai, Regulation of pi-stacked anthracene arrangement for fluorescence modulation of organic solid from monomer to excited oligomer emission, *Chem. – Eur. J.*, 2012, **18**, 4634–4643.

90 J. Feng, X. Wang, L. Wang, J. Kfoury, J. Olah, S. Zhang, L. Zou, Y. Guo and S. Xue, Naphthalimide-Tagged Iron(II) Spin Crossover Complex with Synergy of Ratiometric Fluorescence for Thermosensing, *Inorg. Chem.*, 2024, **63**, 108–116.

91 C.-F. Wang, M.-J. Sun, Q.-J. Guo, Z.-X. Cao, L.-S. Zheng and J. Tao, Multiple correlations between spin crossover and fluorescence in a dinuclear compound, *Chem. Commun.*, 2016, **52**, 14322–14325.

92 S. Ohkoshi, K. Imoto, Y. Tsunobuchi, S. Takano and H. Tokoro, Light-induced spin-crossover magnet, *Nat. Chem.*, 2011, **3**, 564–569.

93 A. Marino, P. Chakraborty, M. Servol, M. Lorenc, E. Collet and A. Hauser, The role of ligand-field states in the ultrafast photophysical cycle of the prototypical iron(II) spin-crossover compound [Fe(ptz)(6)](BF(4))(2), *Angew. Chem., Int. Ed.*, 2014, **53**, 3863–3867.

94 T. Delgado, M. Meneses-Sanchez, L. Pineiro-Lopez, C. Bartual-Murgui, M. C. Munoz and J. A. Real, Thermo- and photo-modulation of exciplex fluorescence in a 3D spin crossover Hofmann-type coordination polymer, *Chem. Sci.*, 2018, **9**, 8446–8452.

95 (*a*) CCDC 2427600: Experimental Crystal Structure Determination, 2026, DOI: **10.5517/ccdc.csd.cc2mh3py**; (*b*) CCDC 2427601: Experimental Crystal Structure Determination, 2026, DOI: **10.5517/ccdc.csd.cc2mh3qz**; (*c*) CCDC 2427602: Experimental Crystal Structure Determination, 2026, DOI: **10.5517/ccdc.csd.cc2mh3r0**;

(*d*) CCDC 2427603: Experimental Crystal Structure Determination, 2026, DOI: 10.5517/ccdc.csd.cc2mh3s1; (*e*) CCDC 2427604: Experimental Crystal Structure Determination, 2026, DOI: 10.5517/ccdc.csd.cc2mh3t2; (*f*) CCDC 2427605: Experimental Crystal Structure Determination, 2026, DOI: 10.5517/ccdc.csd.cc2mh3v3; (*g*) CCDC 2427606: Experimental Crystal Structure Determination, 2026, DOI: 10.5517/ccdc.csd.cc2mh3w4.